Journal of Petroleum Science and Engineering 209 (2022) 109934

Contents lists available at ScienceDirect

Journal of Petroleum Science and Engineering

journal homepage: www.elsevier.com/locate/petrol

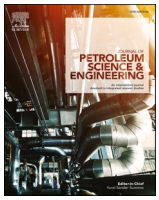

Anisotropic rate-dependent saturation functions for compositional simulation of sandstone composites

Maartje Boon [a,*], Stephan K. Matthäi [b], Qi Shao [b], AbdAllah A. Youssef [b], Achyut Mishra [b], Sally M. Benson [a]

[a] Department of Energy Resources Engineering, Stanford University, CA, USA
[b] Peter Cook Centre for CCS Research, The University of Melbourne, Parkville, VIC 3010, Australia

ARTICLE INFO

Keywords:
Laminations
Rate dependence
Relative permeability
Upscaling
CO_2 plume spreading
Anisotropy

ABSTRACT

Determination of representative saturation functions for permeable reservoir sandstones requires consideration of mm-cm scale laminations and crossbedding common in these heterogeneous porous media. Modelling selected laminated sandstones from CO2CRC's Otway International Test Centre in Victoria, Australia as bimodal composites of different rock types, we analyse drainage relative permeability parallel and perpendicular to the laminae for a range of driving gradients. The results from these numeric drainage experiments are curve fit across a continuous range of flow rates between the capillary and viscous limits. Our analysis shows that laminae-related small, but spatially correlated grainsize and permeability variations give rise to flow-rate dependent drainage behaviour at the bed scale. The flow direction- and rate-dependent behaviour is captured by a new set of anisotropic extended saturation functions that are implemented and presented in a form that is suitable for compositional simulation in the system CO_2–H_2O–NaCl. For the first time, these new constitutive relationships permit an investigation of feedbacks between the reservoir-scale flow regime and bed-scale phase mobility. To illustrate the application of these functions in reservoir simulation, meter-scale plume spreading simulations are presented for a suite of ten homogenised fluvial-to-estuarine sandstones from the Otway facility.

1. Introduction

Relative permeability, $k_{r\alpha}(s_w)$ and capillary pressure, $P_c(s_w)$, subsequently referred to as saturation functions, are fundamental constitutive relations underpinning reservoir simulation (Aziz and Settari, 1979). Although originally derived to interpret the results of slim tube experiments with disturbed samples of reservoir sands (Muskat et al., 1937), today, saturation functions are also applied to predict the flow behaviour of heterogeneous rocks at different scales, including predictions of sweep and micro-displacement efficiency (Lake, 2010). The accuracy of such predictions is key for successful reservoir management and the design and performance assessment of CO_2 geo-sequestration sites. However, the latter typically relies on hysteric models for homogeneous rocktypes (Spiteri et al., 2008) or results from special core analysis (SCAL) of cm-scale samples selected to represent only homogeneous rock types. This selection process implies a sampling bias against visibly non-uniform rocks although these might represent the volumetrically most important facies associations of the net-reservoir rocks at a specific site (Ringrose, 2008; Ringrose et al., 1996).

In the awareness of continuum-scale heterogeneity, upscaling procedures have been developed to translate core-scale measurements to the field scale (Durlofsky, 2005; Jackson and Krevor, 2020). While most of these methods focus on finding meaningful averages for permeability, some also consider multiphase flow and SCAL derived curves. Both numerical (Coll et al., 2001; Jackson et al., 2018; Pickup and Sorbie, 1996) and experimental studies (Manoorkar et al., 2021; Perrin and Benson, 2010; Reynolds and Krevor, 2015) show that continuum-scale heterogeneity has a major influence on multiphase flow. Lohne et al. (2006), Jonoud and Jackson (2008), and Boon and Benson (2021) have shown that fractional flows are not only functions of saturation but are also affected by local force balances such as the ratio of viscous and capillary forces in the rock volume of interest, see Fig. 1. This implies that upscaling makes saturation functions multi-variable anisotropic functions (Ekrann and Aasen, 2000; Odsæter et al., 2015). It is worth pointing out that this multi-variable nature of relative permeability functions was first observed in the context of gas condensate systems

* Corresponding author.
E-mail address: mmboon@stanford.edu (M. Boon).

https://doi.org/10.1016/j.petrol.2021.109934
Received 18 September 2021; Received in revised form 17 November 2021; Accepted 25 November 2021
Available online 27 November 2021
0920-4105/

(Mott et al., 1999,2000; Henderson et al., 1996, 1997,1999; and others). At high velocities near the well bore, the effective relative permeability of the gas phase increases with increasing velocity which has a positive effect on the well productivity. At the same time, at high velocity, inertial (non-Darcy) flow effects reduce the effective gas relative permeability (Mott et al., 2000). It is the counter balance of these two phenomena that determines the overall effect of this rate-dependency on the well productivity of gas condensate systems. At typical gas condensate well flow rates, flow-rate dependency leads to an improvement in the well productivity (Nasriani et al., 2015). Although gas condensate are not the focus of this work, the above example highlights the broader need for a multi-variable framework for saturation functions.

Most upscaling studies derive upscaled parameters for fixed ratios of capillary and viscous forces. Pickup et al. (2000) applied capillary limit (CL) conditions in their model of fluvio-aeolian sandstones and viscous limit approximations (VL) in their model of intertidal-to-deltaic sandstones. For laminated composite rock types, the upscaled relative permeability and upscaled capillary pressure in the VL and CL, can be calculated analytically, for both, the horizontal and vertical direction (Corey and Rathjens, 1956; Odsæter et al., 2015; Rabinovich et al., 2016). For flow rates that fall in between, considering laminated structures, an analytical method to calculate upscaled multiphase flow parameters in the direction across the lamina exists (Dale et al., 1997). Recently, Boon and Benson (2021) presented a physics-based model to calculate flow-rate dependent multiphase flow parameters in the direction parallel to lamina, while (Moreno et al., 2021) developed a model, based on a 1D semi-analytical solution for steady state and not restricted to a specific heterogeneity structure, for calculating rate dependent effective relative permeability curves. All these methods are based on the fractional flow approach and have the potential to form the basis for a more general approach to incorporate flow-rate dependent saturation functions into a reservoir simulator which is the focus of this work.

The current study focuses on the functional form of relative permeability and capillary pressure curves of laminated and cross-bedded composite sandstone, and the modelling of their variability in terms of constitutive relationships for reservoir simulation. Relative permeability was studied by means of physical and numeric steady-state drainage experiments conducted at a spectrum of flow velocities and for two flow directions: parallel and perpendicular to the laminae. Experimental measurements were curve-fitted using a single framework. These curves serve as a basis for a novel anisotropic rate-dependent relative permeability/capillary pressure model that is implemented in a reservoir simulator and used in bed-scale CO_2 plume spreading simulations the results of which are contrasted and compared as a proof of concept at the end of this article.

2. Composite rock types

The physical experiments and numeric sensitivity analysis were conducted on a suite of heterogeneous rock samples from the CRC-3 well at CO2CRC's Otway International Test Centre in Victoria, Australia, where CO_2 injection experiments were conducted from 2008 to 2020 (Cook, 2014; Pevzner et al., 2020), see Table 1. The sedimentary heterogeneity observed in the rock samples consisted of planar bedding, massive bedding, and crossbedding. The thickness of the bedding layers is at the mm-cm scale, while the lateral extent of the layers depends on the depositional environment but is at least one order of magnitude larger than the thickness of the layer (Ringrose et al., 1993).

The test facility lies within the Otway sedimentary basin that contains volcanogenic CO_2 accumulations in a predominantly siliciclastic

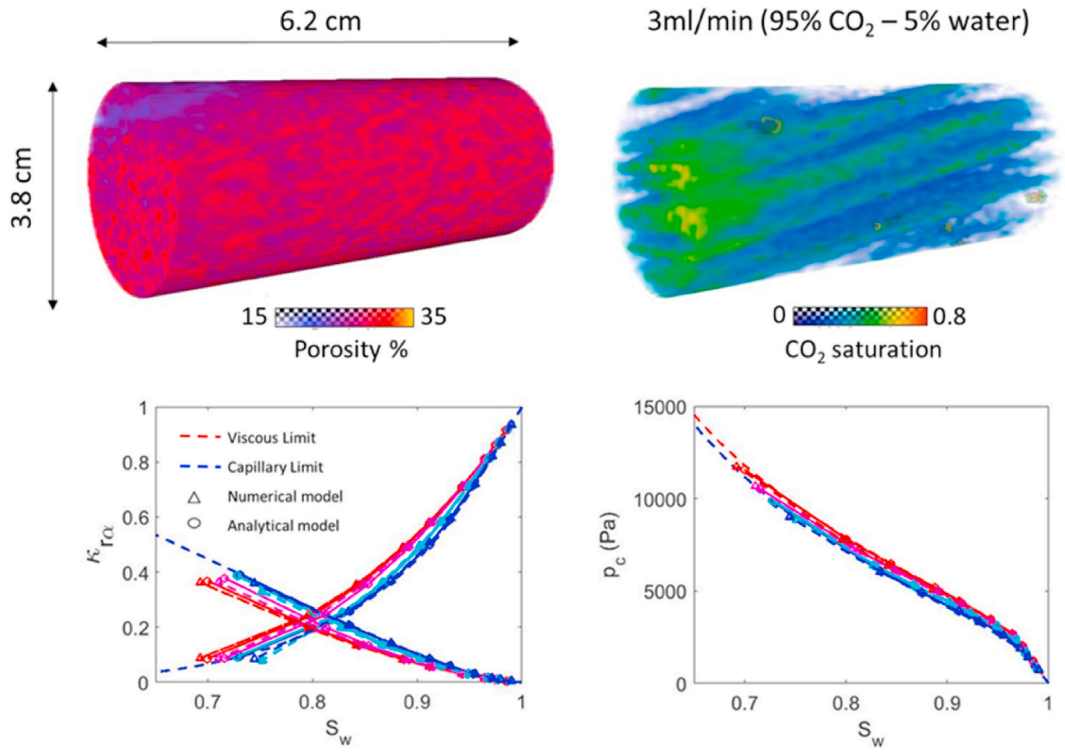

Fig. 1. Laminated sandstone core from the Paaratte FM and the rate-dependent drainage behaviour obtained by combining experimental results with numerical and analytical models (Boon et al., 2021) Top left: porosity map. Top right: CO_2 saturation distribution during drainage at steady state reached for a fractional flow of 95% CO_2 and 5% water. Bottom left: flow-rate dependent relative permeability. Bottom right: flow-rate dependent capillary pressure. Each colour indicates a different flow rate (6.67e-04 m/s, 6.67e-03 m/s, 6.67e-02 m/s, 6.67e-01 m/s). Each circle indicates a different fractional flow ($f_{wr} = 0.01, 0.05, 0.1, 0.2, 0.3, 0.5, 0.7, 0.8, 0.9$). (For interpretation of the references to colour in this figure legend, the reader is referred to the Web version of this article.)

Table 1
Composition and sedimentary structures of composite rock types sampled from Otway well CRC-3 and modelled by Mishra et al.(2020), creating 2D input models for the numeric simulations used to establish the ensemble relative permeabilities reported here.

Rock Type Composition	Sedimentary Heterogeneity	Abbreviation Used
Coarse sandstone and fine sandstone (RT14)	Cross bedding	X^{FSst}_{CSst}
Mudstone and coarse sandstone (RT8)	Planar bedding	P^{Mst}_{CSst}
Mudstone and fine sandstone (RT6)	Planar bedding	P^{Mst}_{FSst}
Siltstone and coarse sandstone (RT12)	Planar bedding	P^{Slt}_{CSst}
Siltstone and fine sandstone (RT11)	Planar bedding	P^{Slt}_{FSst}
Mudstone and siltstone (RT4)	Planar bedding	P^{Mst}_{Slt}
Carbonate-cemented sandstone and coarse sandstone (RT9)	Massive bedding	M^{CbSst}_{CSst}
Carbonate-cemented sandstone and fine sandstone (RT8)	Massive bedding	M^{CbSst}_{FSst}
Carbonate-cemented sandstone and siltstone (RT5)	Massive bedding	M^{CbSst}_{Slt}
Carbonate-cemented sandstone and mudstone (RT2)	Massive bedding	M^{CbSst}_{Mst}

Cretaceous to Quaternary sequence deposited in a fluvial – estuarine - deltaic environment (Geary and Reid, 1998; Mishra et al., 2019). Arguably, the best characterized interval within this sequence, is the Paaratte formation, logged and cored in several wells (Dance et al., 2012; Lawrence et al., 2013), and target of several plume-spreading and geophysical monitoring experiments (e.g, Sharma et al., 2011; Paterson et al., 2013). The Paaratte formation consists of multiple fining-upward sedimentation cycles (parasequences) topped by shales acting as caprocks. In the coarser intervals, sedimentary facies vary rapidly along strike. Elongated channel mouth-bar deposits constitute the most permeable geobodies. The sequence has a normal-to transtensional tectonic overprint manifest in many faults (e.g., Ziesch et al., 2017), and its original properties have been significantly altered by cementation. Where epigenic carbonate nodules formed and horizons were calcified, porosity and permeability were lost (Daniel et al., 2012).

Using a combination of well logs and core samples, Mishra et al. (2019, 2020) characterized the lithological variability of the targeted Paaratte Parasequence 1 (PS1) aquifer in detail, from the centimeter to the hectometer scale. Air minipermeameter logs obtained on the drill core constrain the permeability variation in the PS1. These measurements indicate a bimodal permeability distribution with maxima at 0.1 mD (shale) and 1 D (sandstone), see Fig. 2.

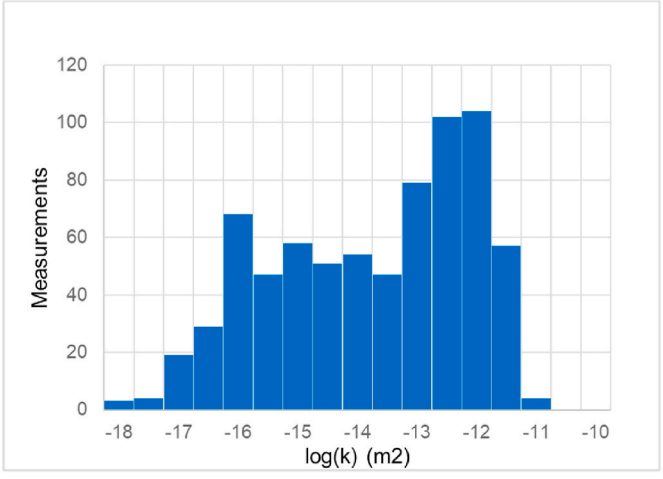

Fig. 2. Bimodal permeability distribution of the laminated composite rocktypes in Paaratte Parasequence 1 as determined by mini-permeameter measurements on the split core, representing moving 2.5 cm averages; n = 726 samples, see also Dance et al. (2019).

Although these extrema are relatively weakly defined (<30% of entire population), they fingerprint the laminated nature of the rocks that is seen clearly in hand specimen. Overall the PS1 is highly heterogeneous as is indicated by its Lorentz permeability index, see Fanchi (2010). Importantly, physical experiments we conducted (Boon et al., 2021) together with the semi-analytical steady-state upscaling model presented in Boon and Benson (2021) show that the rate-dependency in horizontally laminated rock is highly dependent on the lateral extent of the lamina, with the system quickly moving towards the CL when the layers get longer. If the contrasts are larger than ~1.5 orders of magnitude, the less permeable laminations cease to contribute to the layer-parallel flow and the composite behaves like a highly anisotropic rock with a much-reduced total porosity (Huppler, 1970; Honarpour et al., 1995). The results presented here only consider rate-dependence during the drainage process.

This article is organized into five sections. Starting with a description of the properties of the 10 composite rock types, followed by a description of the procedures used in the numeric sensitivity analysis conducted to determine rate-dependency and the curve-fitting of its results, and subsequently the implementation of the new functions and their integration into the Australian CO_2 Geo-Sequestration Simulator (ACGSS) are described. The article proceeds with the description of the rate dependent saturation functions derived for composite rock types at Otway. Finally, application examples are used to illustrate the impact of the rate dependence determined for each rocktype on plume spreading beneath an impermeable cap rock.

3. Methodology

In the following, we describe 1) the properties of the 10 composite rock types, 2) the method employed for the numeric simulation to estimate the ensembled relative permeability, 3) the curve fitting of the results, 4) the use of the curve fits for the generation of new functions for compositional reservoir simulation, and 5) the input models used in this analysis. The curve fitting was performed to integrate results obtained for different flow rates and flow parallel to- and across the laminations in the rock samples. The second part of the methodology describes how we transformed these fits into novel anisotropic functions that employ the parameters flow direction and flow magnitude in addition to the conventional parameter saturation to predict relative permeability and capillary pressure.

3.1. Properties of the composite rock types

The local steady-steady relative permeability and capillary pressure analysis performed in this study discerned 10 composite rocktypes mapped in the Paaratte Parasequence 1 (PS1) that lies within the Otway sedimentary basin in Victoria, Australia (see Mishra et al., 2020, 2019). The composite rocktypes comprise three sedimentary structures: the interface of two massively bedded rock types, planar bedding, and crossbedding (Table 1 & Fig. 3). Each of the composite domains is 0.05m thick and consists of two of the homogeneous rocktypes presented in Table 2. The lateral extent of the lamination is assumed to be on average 0.3 m for the planar bedding and around 1 m for the larger bedforms.

The porosity, permeability and capillary entry pressure values of the five homogeneous rock types are based on previous publications (Dance et al., 2019; Daniel, 2012; Daniel et al., 2012; Lawrence et al., 2013). Results from the MICP experiments (Daniel, 2012; Daniel et al., 2012) are used to calculate the equivalent height of the CO_2 column before the intrusion of CO_2 into the core sample will occur under buoyancy. Under this condition, buoyancy pressure becomes equal to the capillary entry pressure (P_e) (Kaldi et al., 2011), and the following expression can be

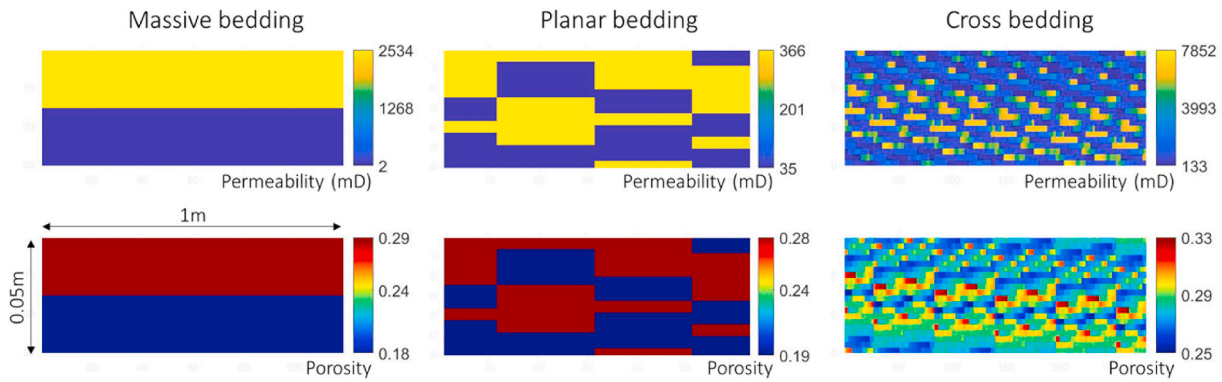

Fig. 3. Permeability and porosity maps of three composite rocktypes with different sedimentary structures Left: Carbonate-cemented sandstone and mudstone (RT2) containing massive bedding. Middle: Siltstone and fine sandstone (RT11) containing planar bedding. Right: Coarse sandstone and fine sandstone (RT14) containing crossbedding (Table 1).

Table 2
Rock properties of the five homogeneous rock types for the CO2CRC's Otway Research Facility site. P_e is the capillary entry pressure [Pa], S_{wr} is the irreducable water saturation, and m is the VanGenuchten parameter.

Rock Type	Abbreviation	Porosity	Permeability (mD)	P_e (Pa)	S_{wr}	m
Coarse sandstone	CSst	0.286	2534	750	0.104	0.7
Fine sandstone	FSst	0.28	365.5	1000	0.159	0.6
Siltstone	Slt	0.19	35.22	3000	0.180	0.5
Mudstone	Mst	0.176	1.750	5000	0.390	0.4
Carbonate-cemented sandstone	CbSst	0.176	1.560	10000	0.552	0.4

used for the calculation of P_e values of each of the homogeneous rock types,

$$P_e = \Delta\rho g h, \tag{1}$$

where, $\Delta\rho$ is the density difference between brine and supercritical CO_2 [kg/m^3], g is the gravitational acceleration [m/s^2], h is the height of CO_2 above the free water level [m]. The empirical VanGenuchten exponent m for each rock type was taken from the literature (Cheng et al., 2017; Hermanson and Kirste, 2013). The irreducible water saturation, S_{wr}, values were calculated using the following empirical relation (Holtz, 2002),

$$s_{wr} = 5.159\left(\frac{\log(k)}{\varphi}\right)^{-1.1559} \tag{2}$$

where, k is the intrinsic permeability [mD] and ∅ is the porosity [-]. The VanGenuchten Mualem-hybrid functions, given by

$$k_{rw} = \begin{cases} 0 \forall 0 \le s_w \le s_{wr} \\ \sqrt{s_w^*}\left[1-\left(\left(1-s_w^*\right)^{1/m}\right)^m\right]^2 \forall s_{wr} < s_w \le 1 \end{cases} \tag{3}$$

$$k_{rnw} = \begin{cases} 1 \forall 0 \le s_w \le s_{wr} \\ \left(1-s_w^*\right)^2\left(1-\left(s_w^*\right)^2\right) \forall s_{wr} < s_w \le 1 \end{cases} \tag{4}$$

$$P_c = P_e\left(1-\left(s_w^*\right)^{-1/m}\right)^{1-m} \qquad \forall s_{wr} < s_w \le 1 \tag{5}$$

where, $S_w^* = \frac{S_w - s_{wr}}{1-S_{wr}}$, are used to describe the relative permeability and the capillary pressure functions for each of the homogeneous rocktypes. This work is part of a broader study where next to the impact of heterogeneity in transport, the impact of chemical heterogeneity on the migration and trapping of the CO_2 plume is considered. To stay consistent, the same saturation functions were used in the different studies. The choice for the VanGenuchten hybrid functions was based on the capabilities of the reactive transport code TOUGHREACT (Xu et al., 2008). The disadvantage of VanGenuchten type capillary pressure equations is that at $P_c(S_w = 1) = 0$, as such it does not form a capillary barrier. However, in this study the capillary barrier is taken into account by setting the relative permeability of the CO_2 phase to zero until a critical CO_2 saturation is reached. This is discussed in Section 3.3.2.

3.2. *Steady-state numeric analysis of relative permeability and capillary pressure*

To find flow-rate dependent relative permeability and capillary pressure, numerical flow experiments were carried out for pressure gradients applied in orthogonal directions; one in the horizontal (x-direction) and the other one in the vertical (y-direction) direction at the scale of the rectangular quadrilateral elements (1 m by 0.05 m) of the high-resolution cross-sectional model (not shown).

The relative permeability determination method used is akin to the Penn-State steady-state laboratory method for the determination of relative permeability (Osoba et al., 1951) which determines the pressure gradient of CO_2 and water and the saturation of the sample following constant-rate co-injection of CO_2 and water at a range of fractional flows.

A commercial reservoir simulator, Eclipse-100, was used to upscale the flow behaviour seen in the core plugs to the domain target scale (Fig. 3). Eclipse-100 is a fully-implicit, three phase, three dimensional, general purpose oil and gas reservoir simulator which solves the black oil equations on corner-point grids. In the core-scale simulations, it was assumed that gravitational forces could be neglected as compared with both capillary and viscous forces (Pickup et al., 2000). However, instead of assuming a dominance of capillary over viscous forces, the numerical experiments were conducted to cover a range of plausible force balances. At very low total velocities (~meters per year), capillary spreading dominates over forced convection and the capillary limit (CL) is reached. A quasi-steady state saturation is attained where the capillary pressure becomes constant across the sample domain. In this case, the CL saturation distribution can be calculated from the inverse of the capillary pressure function $[s_w = P_c(s_w)]$ (e.g., Ekrann et al., 1996). The viscous limit (VL) case of high total velocity is often treated as synonymous with viscous forces dominating over all other forces. The

corresponding VL saturation distribution can be inferred under the assumption that fractional flow is constant along streamlines [$s_w = f_w(s_w)$]. This distribution is therefore entirely dependent on the fractional flow at the inlet boundary. The most widely used inlet condition is constant fractional flow (Ekrann and Aasen, 2000).

The determination of the flow-rate dependent horizontal and vertical flow parameters of the composite rocktypes of Table 1 involved numeric multiphase flow experiments using a similar approach as presented in Krause and Benson (2015). In this approach, CO_2 is injected at a range of fractional flows and flow rates into a 2D domain initially fully saturated with brine. The model inlet is subjected to a constant rate boundary condition, while the outlet is maintained at a constant pressure. No-flow boundaries are applied at the top and bottom. To establish more realistic flow conditions at the inlet, a pillar of highly permeable cells, analogous to a porous plate used in a physical experiment, is inserted. This modification allows fluid phases to distribute and focus into the more permeable parts of the model, see schematic model in Fig. 4. Simulations are run, for each fractional flow, until the steady-state condition is reached. Now the upscaled pore-volume weighted capillary pressure and upscaled pore-volume weighted saturation are calculated. The effective relative permeability (k_r^{eff}) is calculated inserting the phase-pressure gradient into the extended Darcy's law.

3.3. Curve-fitting procedure

3.3.1. Relative permeability

To capture the anisotropic and rate dependent behaviour, relative permeability curves for both wetting and non-wetting phases were fitted with Chierici's exponential model (Chierici, 1984),

$$k_{rw_i}^{eff} = \begin{cases} 0 \forall 0 \le s_w \le s_{wr} \\ e^{-\gamma_{w1_i} R_{w_i}^{-\gamma_{w2_i}}} \forall s_{wr} < s_w \le 1 \end{cases} \tag{6}$$

where $R_{w_i} = \frac{s_w - s_{wr}}{1 - s_w}$, and γ_{w1_i}, γ_{w2_i}, γ_{nw1_i} and γ_{nw2_i} are coefficients fitted with the equation,

$$\gamma_i = \frac{a_i}{1 + b_i |u_i|^{c_i}} + d_i, \tag{8}$$

taking total velocity components (u_i) as input parameters. Here, the subscript i is either the horizontal ($i = x$) or vertical direction ($i = y$). The coefficients in Eqs. (6) and (7) are all empirical coefficients determined by the nonlinear regression on the sets of numerical data points. Their values vary not only between wetting and non-wetting phases, but also between horizontal and vertical directions. All coefficient values for the rate-dependent composites can be found in the supporting information, as well as the root mean square error as function of velocity for all the curve fits of each of the rocktypes.

Based on the flow dynamics observed in the numeric sensitivity analysis, the relative permeability for the horizontal (x) direction for the rock types with the massive bedding can be modelled using the CL solution. The long characteristic lateral correlation length of the massive bedded rock types minimizes the transition saturation zone (rate dependent zone) near the inlet. Further downstream, the saturation distribution is controlled by capillary pressure ($\nabla p_c = 0$) and consequently does not change with flow-rate. (Ekrann and Aasen, 2000). For these massive bedded rock types, the capillary pressure curves as well as the relative permeability in the horizontal direction were calculated analytically (Boon and Benson, 2021; Corey and Rathjens, 1956; Odsæter et al., 2015; Rabinovich et al., 2016). Then, the VanGenuchten Mualem-hybrid model (Eqs. (3)–(5)) is employed to fit the effective saturation functions.

3.3.2. Capillary pressure

Since pressure is a scalar variable, capillary pressure must be isotropic. To capture the flow-rate dependent isotropic behaviour observed for the composites, the VanGenuchten curves were fitted to the capillary pressure determined during the horizontal numeric flow experiments. The Van Genuchten P_c curves are used as follows

$$P_c(s_w) = \begin{cases} \min\left(P_c(s_{wr} + 0.01) + \left.\frac{dP_c}{ds_w}\right|_{s_w = s_{wr} + 0.01} (s_w - s_{wr} - 0.01),\ P_{c_{\max}} \right) & \forall 0 \le s_w < s_{wr} + 0.01 \\ P_0 \left(1 - \left(s_w^*\right)^{-1/m}\right)^{1-m} & \forall s_{wr} + 0.01 \le s_w \le 1 \end{cases} \tag{9}$$

$$k_{rnw_i}^{eff} = \begin{cases} 1 \forall 0 \le s_w \le s_{wr} \\ e^{-\gamma_{nw1_i} R_{w_i}^{-\gamma_{nw2_i}}} \forall s_{wr} < s_w \le 1 \end{cases} \tag{7}$$

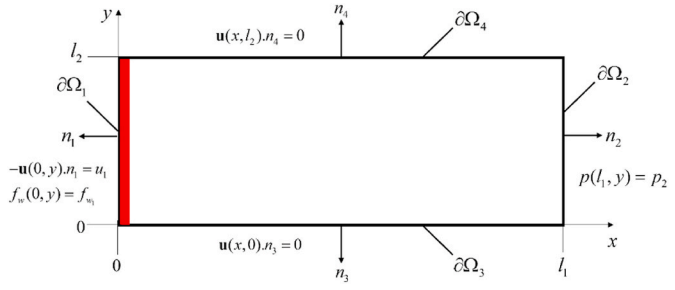

Fig. 4. Model setup for local steady-state analysis of relative permeability on the metre scale in the horizontal direction. The high permeability inlet region is shown in red. (For interpretation of the references to colour in this figure legend, the reader is referred to the Web version of this article.)

where P_0 is an empirical coefficient and $P_{c_{\max}} = 10^7$ Pa is set as an upper limit on capillary pressure. Without this limit, Eq (9) gives infinite value at s_{wr}. Also, the applicability of the VanGenuchten formula is limited to saturations that are higher than s_{wr} by at least 0.01. Moreover, in compositional simulation it is expected that water evaporates into the CO_2 phase leading to decreasing s_w below s_{wr}. To deal with such saturation states the following linear extension for P_c is used below $s_{wr} + 0.01$. To define a reasonable capillary pressure gradient over the whole saturation range, $\frac{dP_c}{ds_w}$ for saturation range below $s_{wr} + 0.01$ is set to $\left.\frac{dP_c}{ds_w}\right|_{s_w = s_{wr} + 0.01}$. Such definition assures the continuity of the capillary pressure gradient, which controls the capillary spreading, and avoid having zero gradient if the gradient is estimated using Eq (9) directly. The rate dependency is introduced into these curves via a flow velocity dependent P_0 value as follows

$$P_0 = \frac{a}{1 + b|u_x|^c} + d \tag{10}$$

As stated previously, For the massive bedded rocktypes, which do not

show the impact of flow-rate dependency in the horizontal direction, P_0 is taken as a constant.

3.3.3. Capillary barrier

Since capillary pressure is isotropic, the same capillary pressure curves will be used dependent on the flow rate in the horizontal direction, irrespective of the actual flow direction. However, for the flow across the layers (flow in y direction), the low permeable layers may form a capillary barrier. To take this into account, we create a barrier through the relative permeability of the non-wetting phase in the y direction by setting the layer crossflow relative permeability of CO_2 to zero for water saturations higher than the threshold saturation (s_{wt}). The lower bound of s_{wt} in the CL is s_{wt_CL} , the saturation of the composite at the threshold capillary pressure. It is taken as the highest entry pressure of the composite components. The value of s_{wt} increases with $|u_y|$ reaching 1 at the VL ($s_{wt\_VL} = 1$). It is estimated as follows,

$$s_{wt} = \frac{s_{wt\_CL}}{1 + b|u_y|^c}, \tag{11}$$

where b and c are the parameters used earlier to estimate γ_{nw1_i}. The parameter, R_{w_y} that was used to estimate $k^{eff}_{rnw_y}$, is modifed to be rate-dependent as follows,

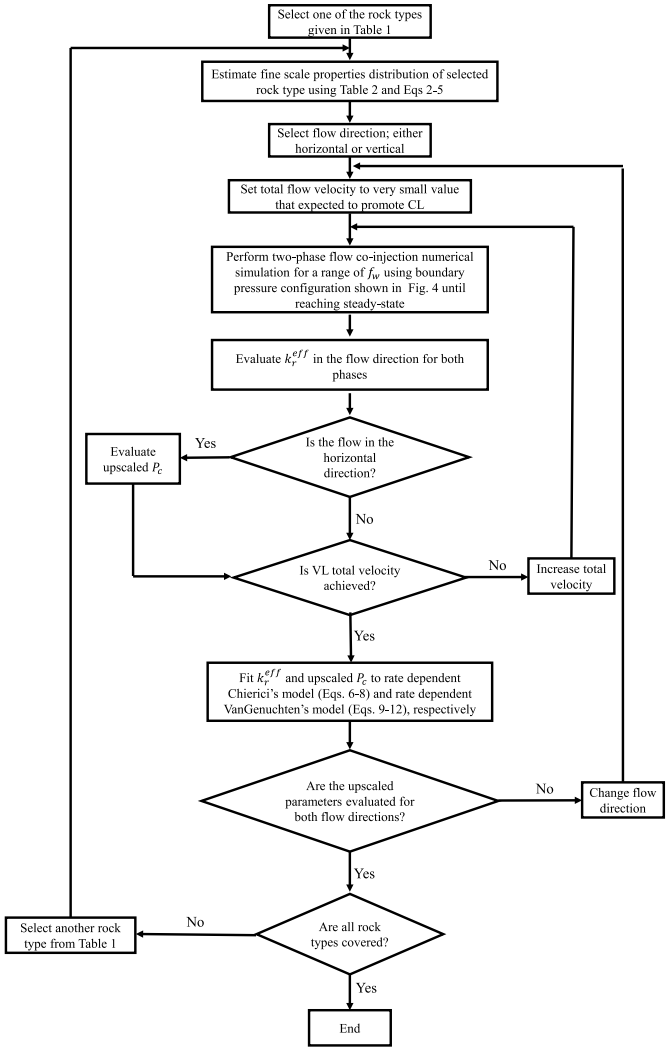

Fig. 5. Flow chart of the construction of curve-fitted rate-dependent saturation functions based on numerical flow experiments.

$$R_{w_y} = \frac{s_w - s_{wr}}{s_{wt} - s_w}, \tag{12}$$

while all the remaining calculations are exactly as explained previously.

The flow chart shown in Fig. 5 visualizes the construction algorithm of the curve-fitted rate-dependent saturation functions of the composite rock types. In summary, the described approach rests on the following assumptions:

- The anisotropic relative permeability can be obtained from the analysis of flows parallel and perpendicular to the laminations.
- In the CL, the saturation in each sublayer is uniform and determined only by the capillary pressure curve for the ensemble.
- In the VL, the fractional flow across the model is assumed to be uniform. In this case that may be common for highly permeable sandstones, the viscous drag that the flowing phases exert on one-another is ignored. Thus, capillary desaturation (Lake, 2010) at high flow rate is ignored.
- Gravity effects on saturation are ignored.
- Ensemble relative permeability changes instantaneously with flow rate (no scanning curves).
- Only the relative permeability is considered as anisotropic, not capillary pressure.
- A smooth, gradual transition of relative permeability between the viscous and capillary limit is assumed.

3.4. Implementation of functions into reservoir simulators

To the best knowledge of the authors, none of the commercial reservoir simulators supports rate-dependent relative permeability. To overcome this issue, the anisotropic, rate-dependent saturation functions were implemented in the Australian CO_2 geo-sequestration simulator (ACGSS) that is based on the Complex Systems Modelling Platform (CSMP++, Matthäi et al., 2007) as well as the finite element-centered - finite volume simulator (FECFVM, Bazrafkan et al., 2014) for trial simulations in 2D, see further below. The FECFVM method uses unstructured collocated finite element and finite volume meshes and an IMPES operator-splitting approach to solve the parabolic pressure equation with the FEM and the hyperbolic saturation-transport equation with the FVM. The following section describes the governing equations and their discretization including anisotropic relative permeability.

3.5. Governing equations

The two-phase flow equations solved in the illustrative model are derived by substitution of extended Darcy's law (Muskat, 1938) into the continuity equation. Considering viscous, capillary, and gravitational forces, laminar creeping flow in the pore space is modelled by the system of equations

$$\left\{ \begin{array}{l} \varphi \dfrac{\partial s_\alpha}{\partial t} = \nabla.\left(\overline{\overline{k^G \lambda^G_\alpha}}.\nabla(P_\alpha - \rho_\alpha g D)\right) \\ P_c = P_{co_2} - P_w \\ s_{co_2} + s_w = 1 \end{array} \right\} \forall(\mathbf{x} \in \Omega) \cap (t > 0), \tag{13}$$

where G refers to geo-cellular scale, $\overline{\overline{\lambda}} = \overline{\overline{\frac{k^G}{\mu}}}$ is the mobility tensor, D is depth (positive downward) and $\mathbf{x}$ the space vector. Summation of CO_2 and water volumes generates a divergence free total velocity equation,

$$\nabla.\sum_\alpha \left(\overline{\overline{k^G \lambda^G_\alpha}}.\nabla(P_\alpha - \rho_\alpha g D)\right) = 0 \qquad \forall(\mathbf{x} \in \Omega) \cap (t > 0). \tag{14}$$

Eq (14) includes both P_{co_2} and P_w. To solve only for one pressure, the two most widely used simplification approaches are the global pressure- and the phase-pressure approach (Chen et al., 2006). Herein, the global pressure formulation has been adopted.

Is the global pressure approach applicable to the problem of interest? - Global pressure, P, is defined in terms of P_{co_2}, P_c and the fractional flow of water $\left(f_w = \frac{\lambda_w}{\lambda_w+\lambda_{co_2}}\right)$,

$$P = P_{co_2} - \int \left(f_w \frac{dP_c}{d_{sw}}\right) ds_w \tag{15}$$

Although Eq. (15) reduces the strength of the coupling between pressure and saturation equations by eliminating P_c from the pressure equation, this definition is only suitable for scalar fractional flows (non-directional relative permeability). To reach to a similar form of the pressure equation in the presence of tensorial fractional flow, the global pressure gradient needs to be defined as follows

$$\nabla P = \nabla P_{co_2} - \overline{\overline{f_w}}.\nabla P_c. \tag{16}$$

This tensorial form of the fractional flow is defined as $\overline{\overline{f_\alpha}} = \overline{\overline{\lambda_T}}^{-1}\overline{\overline{\lambda_\alpha}}$. Although the definition in Eq. (16) looks acceptable, it is important to test whether it satisfies the compatibility condition (equality of mixed derivatives) such that it can be considered a valid representation of a gradient field. Considering a diagonal fractional flow, the compatibility condition requires the reciprocity of the mixed derivatives as follows

$$\partial_{xy} P = \partial_{yx} P. \tag{17}$$

Simple mathematical manipulation shows that this equality is satisfied only if Eq (16) describes a general vector field as opposed to a gradient field. Therefore, the global pressure formulation cannot handle tensorial relative permeability unless $\overline{\overline{\lambda^G}}$ is a scalar quantity. In our analysis, however, $\overline{\overline{k_r^G}}$ generated from the composites, is a diagonal tensor. In this case, $\overline{\overline{k_r^G}}$ can be approximated as a scalar quantity (k_r^G) as follows

$$k_r^G \sim k_{rx}^G \frac{\left(u_x^G\right)^2}{\left(u_x^G\right)^2 + \left(u_y^G\right)^2} + k_{ry}^G \frac{\left(u_y^G\right)^2}{\left(u_x^G\right)^2 + \left(u_y^G\right)^2}. \tag{18}$$

Hence, the global pressure formulation can be applied in our IMPES scheme. However, equation (16) amounts to a treatment of only the diagonal components of the tensor and no further investigation of its accuracy is performed in this article.

Back substitution of global pressure, capillary pressure and Eq (18) into Eq (14) yields the corresponding form of the pressure equation

$$\nabla.\left[\overline{\overline{k^G}}.(\lambda_T \nabla P - g(\lambda_{co_2}\rho_{co_2} + \lambda_w \rho_w)\nabla D)\right] = 0 \qquad \forall(\mathbf{x} \in \Omega) \cap (t > 0). \tag{19}$$

Equation (15) is solved for nodal pressure using the standard Galerkin FEM. However, saturation dependent parameters are taken from the previous time step as well as $\mathbf{u}_T^G$ for the rate-dependent composite rock types. This miniscule lag in time is accepted as the saturation change is limited to a user-defined threshold keeping the discretization error within an acceptable range (Bazrafkan et al., 2014). The linear system of the pressure equations is solved with the algebraic multigrid method SAMG (Stüben, 2007). After solving for$P$, the phases velocities at the finite-volume facets are reconstructed as

$$\begin{aligned} \mathbf{u}_{co_2} &= -\overline{\overline{k^G}}\lambda_{co_2}.(\nabla P + f_w \nabla P_c - \rho_{co_2} g \nabla D) \qquad \mathbf{u}_w \\ &= -\overline{\overline{k^G}}\lambda_w.(\nabla P - f_{co_2}\nabla P_c - \rho_w g \nabla D) \end{aligned} \tag{20}$$

In the FECFVM, saturation is discretised as piecewise constant on the finite elements and is calculated from the solution of the transport equation [Eq (14)]; total velocity $\mathbf{u}_T$ is post-processed as the sum of the phase velocities and used to update the rate dependent saturation functions.

4. Results

In the previous section a workflow was presented that can be used to incorporate the impact that sub-grid scale laminae have on CO_2 migration into larger scale systems. For this purpose the composite rocktypes of the Paaratte Fm at the Otway site were used. As guidance for the reader, the main steps of this workflow are presented in Fig. 6. The results of each step of the workflow will be discussed in detail in the subsequent sub-sections.

4.1. Function coefficients and forms

While no rate-dependency was observed for the massive bedded rocktypes for layer-horizontal flow, for layer-perpendicular flow significant flow-rate dependence can be seen for RT5, RT7 and RT9. (Fig. 7). For RT2 which consists of layers of carbonate cemented sandstone and mudstone, the least amount of flow-rate dependency and anisotropy can be observed, i.e., the shape of the curves is the same for both flow directions. This is due to the similarity of the two rock-types in both dynamic and static parameters. The shape of the curves is very different for the vertical direction, compared to the horizontal direction for the cases where the members of the composite rocktypes have very different characteristics, such as RT9 which consists of layers of carbonate cemented sandstone and coarse sandstone. In these cases, the cross-over point between the relative permeability curves of the CO_2 and water phase is very low indicating that there is a lot of apparent interference between the two fluids.

All massive bedded rocktypes have a capillary pressure curve with a relatively low entry pressure, reflecting the large size of the pores within these sandstones that were not infilled by the carbonate cement. As shown in Fig. 7, their irreducible brine saturations are very high (>40%), reflecting the fact that the small pores are bypassed by the CO_2 phase. In the vertical direction, the increase in the contrast of the entry pressure between the two members of composites increases s_{wt_CL}. This means that the carbonate-cemented sandstone works as a seal which prevents ingress of CO_2 from the low entry pressure member. This is also reflected in a sharp decline of $k_{rmw_y}^{eff}$ with slight increase in s_w above s_{wr}.

For planar bedded and cross-bedded rocktypes, anisotropic flow-rate dependent behaviour is observed in the horizontal and vertical direction (Fig. 8). As for the massive bedded rocktypes, anisotropy and flow-rate dependence are most apparent in composite rocktypes with members with very different characteristics, such as RT8 which consists of coarse sandstone and mudstone laminations and RT12 which consists of coarse sandstone and siltstone. However, for the cross-bedded fine sandstone and coarse sandstone (RT14), the curves for both directions are very similar and not much flow-rate dependence is observed. Both the fine sandstone and coarse sandstone are very permeable and have a low capillary entry pressure making it easy for the CO_2 to enter both members. Furthermore, it can clearly be seen that the flow-rate dependent behaviour is much more apparent for flow in the vertical direction, i.e., there is a big difference between the CL and the VL curves. The cross-over point between the relative permeability curves of both members in the vertical direction decreases with decreasing flow rate, indicating an increased interference of the two fluid phases obstructing the flow.

Low permeable layers can act as capillary barriers in the case of vertical flow. This has been considered by setting the relative permeability of CO_2 to zero for water saturations higher than the threshold saturation for layer crossflow (Fig. 9). The CO_2 saturation below which this occurs decreases with increasing total velocity, reflecting the shifting balance between viscous and capillary forces. This phase mobilization is controlled by the difference in the capillary entry pressures of the lamina of the composite rocktype. It follows that this behaviour is similar to capillary desaturation observed in experiments with sandstones, studying enhanced oil recovery (CDC curves of Lake, 2010). Importantly, by contrast to single lithology rocktypes, whose

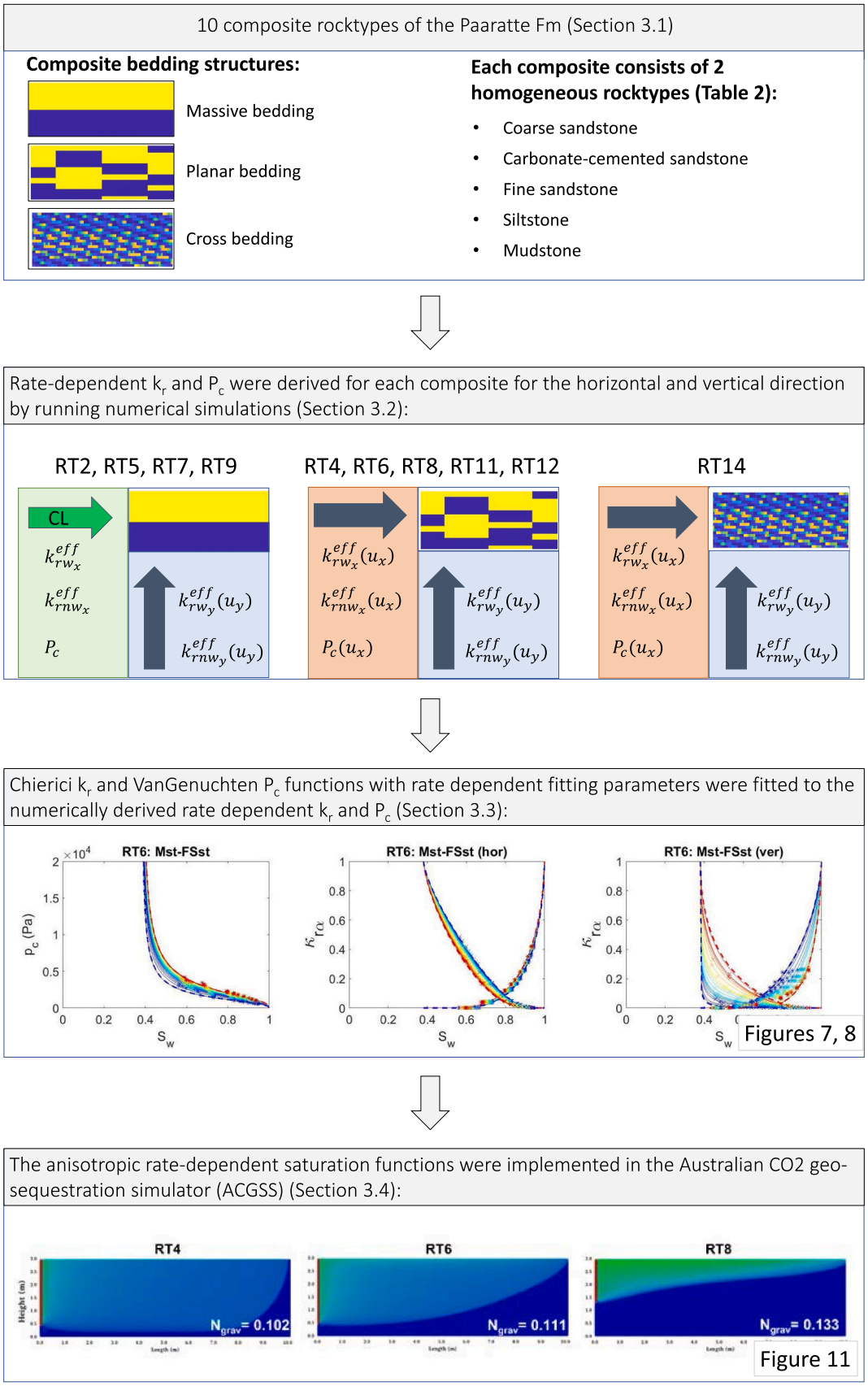

Fig. 6. The main steps of the workflow that was presented in Section 3 to incorporate the impact of sub-grid scale lamina on CO_2 migration into larger scale systems. For this purpose the composite rocktypes of the Paaratte Fm were used.

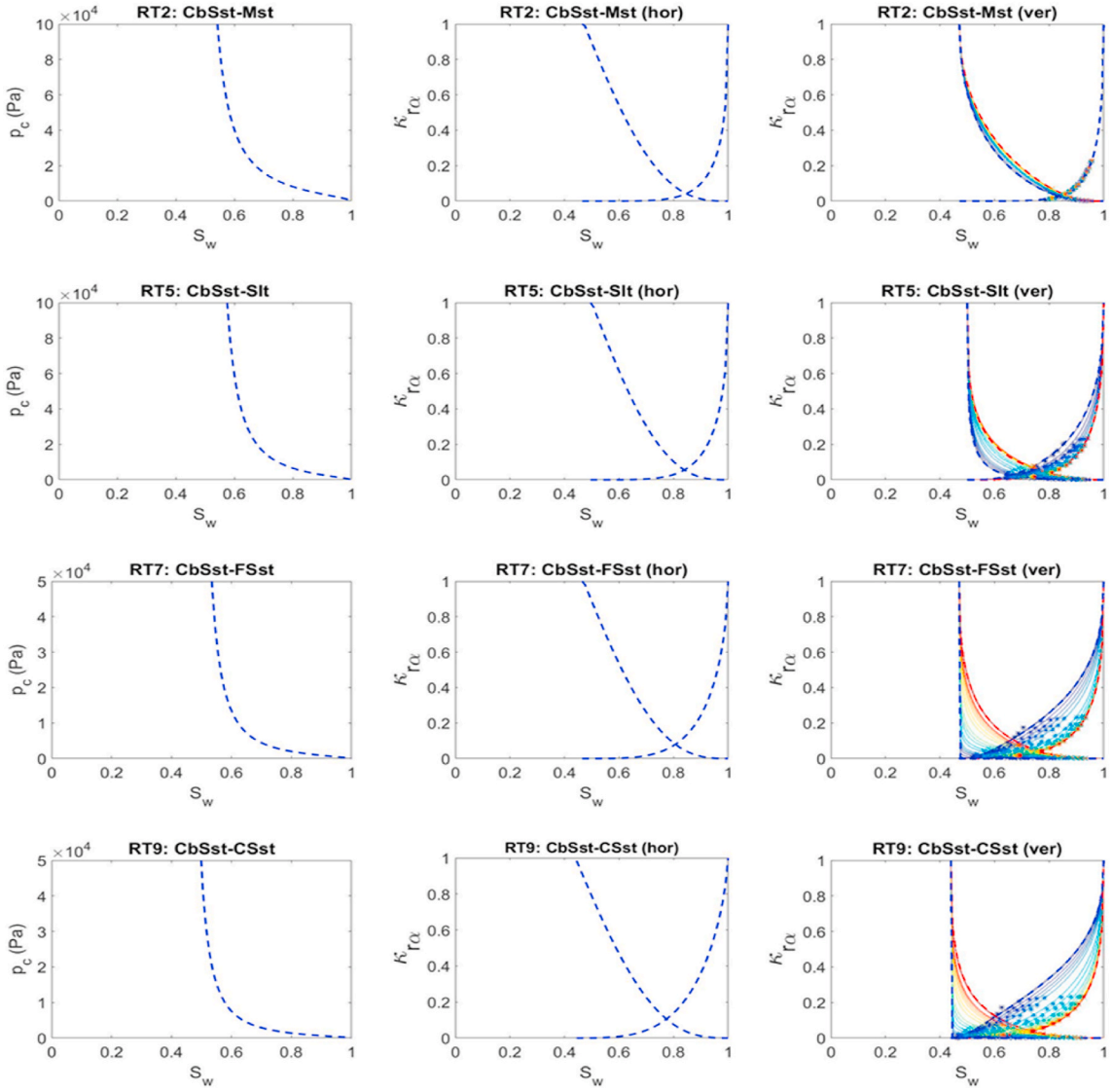

Fig. 7. Ensemble saturation functions for the rocktypes RT2, RT5, RT7, RT9. Drainage capillary pressure curves (left), ensemble relative permeabilities curves for flow in the horizontal direction in the CL (centre), flow-rate dependent ensemble relative permeabilities for flow in the vertical direction (right). The blue and red dashed lines represent the CL and VL cases, respectively. The colours indicate different flow rates ranging between 9.88e-09 m/s and 4.43e-03 m/s. The stars and crosses are the simulation results. The solid lines mark the results of the curve fits. (For interpretation of the references to colour in this figure legend, the reader is referred to the Web version of this article.)

interfaces with neighbouring lithologies coincide with potential discontinuities in capillary pressure, the abstraction of the composite types into ensembles means that the effect of multiple interfaces is averaged, turning entry pressure discontinuities into a sharp transition zone in the model with a thickness of the corresponding composite layer. This abstraction rationalises the modelling of capillary threshold behaviour via the relative permeability curves.

When the flow regime moves from the CL to the VL, effective saturation changes in addition to the fine scale saturation distribution. For flow in in the horizontal direction, the transition from the CL to the VL begins at a much higher velocity than in the vertical direction (Fig. 10). In addition to the flow-direction, this transition velocity depends on the strength of the capillary flux and, consequently, on the thickness of the laminations in the composite rocktype as it is a function of the gradient of the capillary pressure in the rock. The average capillary flux in RT2 (carbonate-cemented sandstone-mudstone), is much weaker than in RT9 (carbonate cemented sandstone-coarse sandstone) because capillary pressure differences are smaller. Therefore, the transition from the CL to the VL in the vertical direction occurs at lower flow velocities than for RT2. By contrast, the cross-bedded sandstone RT14 transitions from the VL to the CL at higher velocities because the layers are thin, and its effective permeability is high. An interesting observation is that for RT14 and flow in the horizontal direction, the increase in saturation with decreasing flow rate is not monotonic (Fig. 10). This will be revisited in the discussion.

4.2. *Plume spreading simulations with rate-dependent rocktypes*

The performance of the newly implemented ensemble saturation functions was evaluated in reservoir simulations with a single rocktype model, one by one, ascertaining robustness, consistency with the prescribed end-point saturations, and for gaining a first impression how the curves manifest themselves in CO_2 plume spreading patterns. The simulations were conducted with the FECFVM simulator (Bazrafkan et al., 2014) and setup such that the petrophysical properties of each model represent the equivalent properties of the corresponding rock type including the composites. The runs simulate linear plume spreading in a cross section. For PT conditions like those used in the upscaling

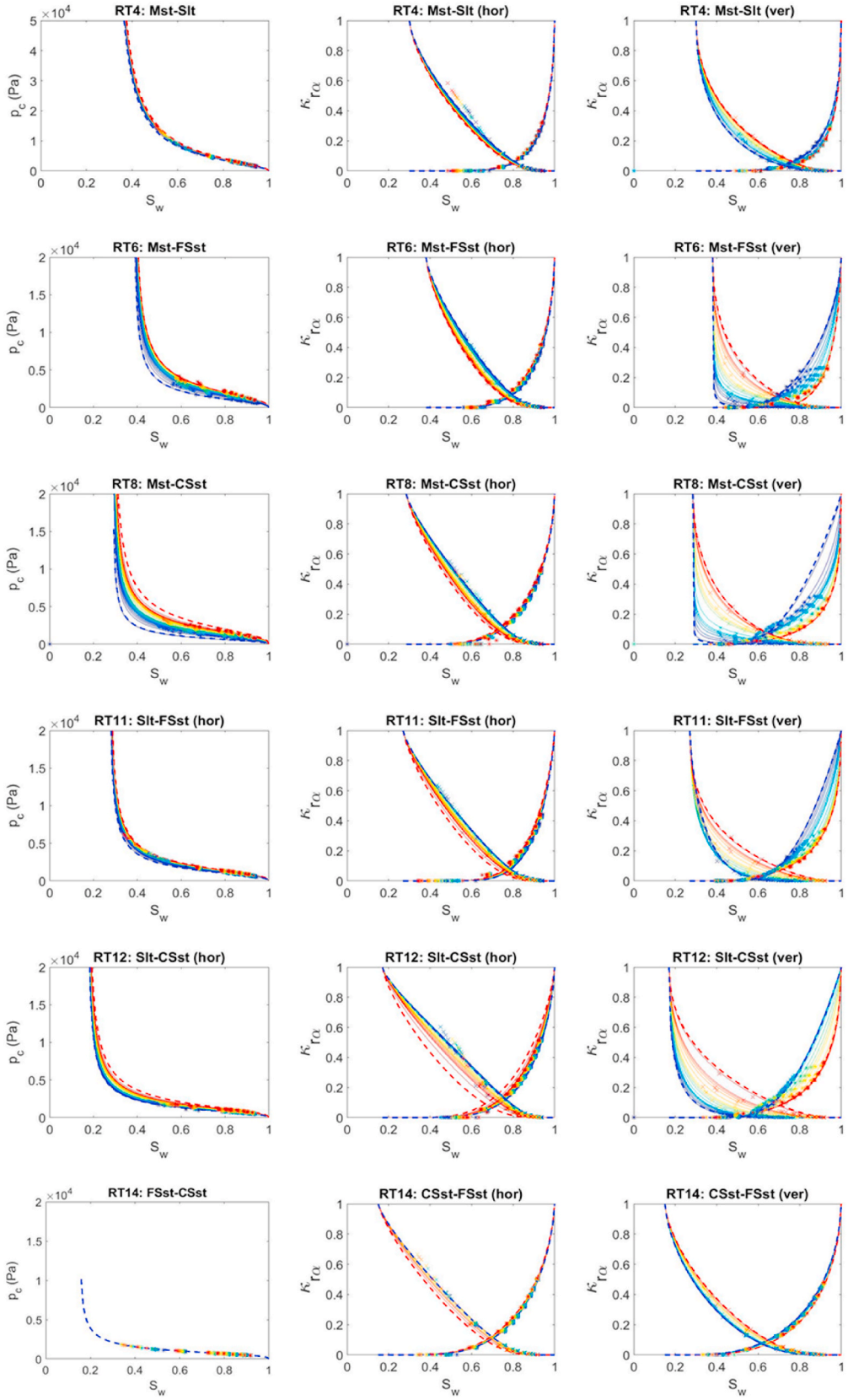

Fig. 8. Upscaled relative permeability (right and middle columns) and capillary pressure curves (left column) for anisotropic rate-dependent planar bedded and cross-bedded rock types. Blue and red dashed lines mark CL and VL. The colours indicate different flow rates. For the planar bedded rocktypes the flow rates ranged between 2.22e-06 m/s and 8.88e-03 m/s, and 1.74e-09 and 1.74e-03, for the horizontal and vertical direction, respectively. For the cross bedded rocktype 14 the flow rates ranged between 1.33e-06 m/s and 2.67e-02 m/s, and 6.72e-07 m/s and 2.68e-03 m/s, for the horizontal and vertical direction, respectively. Stars and crosses mark simulation results while solid lines are the curve fits. (For interpretation of the references to colour in this figure legend, the reader is referred to the Web version of this article.)

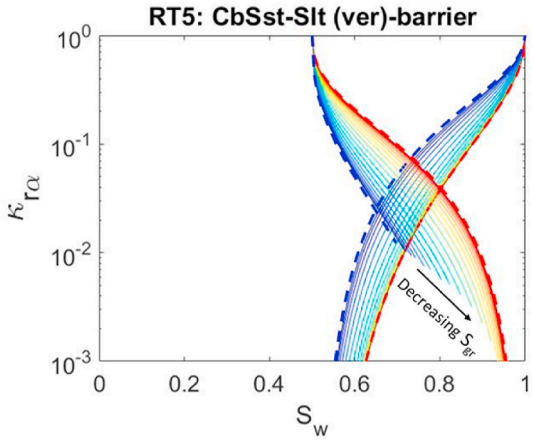

Fig. 9. Capillary barrier created by setting CO_2 relative permeability to zero for $S_w > S_{wt}$. This threshold saturation increases with flow-velocity. Blue and red dashed lines mark CL and VL. Rainbow coloured lines indicate flow rate ranging between 9.88e-08 m/s (blue) to 2.00e-03 m/s (red). (For interpretation of the references to colour in this figure legend, the reader is referred to the Web version of this article.)

computations, supercritical CO_2 was injected through a highly permeable vertical well on the left endowed with linear flow laws, observing how it enters through the sandface and spreads in the rocktype. Different injection rates were applied to trigger flow behaviour between the capillary and viscous limits (Fig. 11). Since these are 2D simulations, the force balances do not vary with increasing distance from the injector.

For the results shown in Fig. 11, the injection flux through the well was fixed at $10^{-5}\,\frac{m^3/s}{m^2}$ for all rocktypes while the right boundary was kept at a fixed pressure fluid static pressure. Immediate gravity segregation occurs in the well before the CO_2 enters the formation. The free CO_2-water level in the well reflects the injection rate and the ease at which the supercritical carbon dioxide can enter the formation (cf., Paterson et al., 2016). The chosen injection rate leads to a viscous to gravitational force balance described by, $\left(N_{grav} = \frac{k_y g \Delta\rho}{\mu_{CO2} u_{Tx}}\right)$ with implications for the areal sweep. It can be seen, however that although RT7 and RT9 have the same N_{grav}, they show a very different areal sweep. This reveals the non-intuitive impact of the flow regime on the sweep when it is allowed to feedback into the saturation functions.

5. Discussion

Relative permeability and capillary pressure in homogeneous

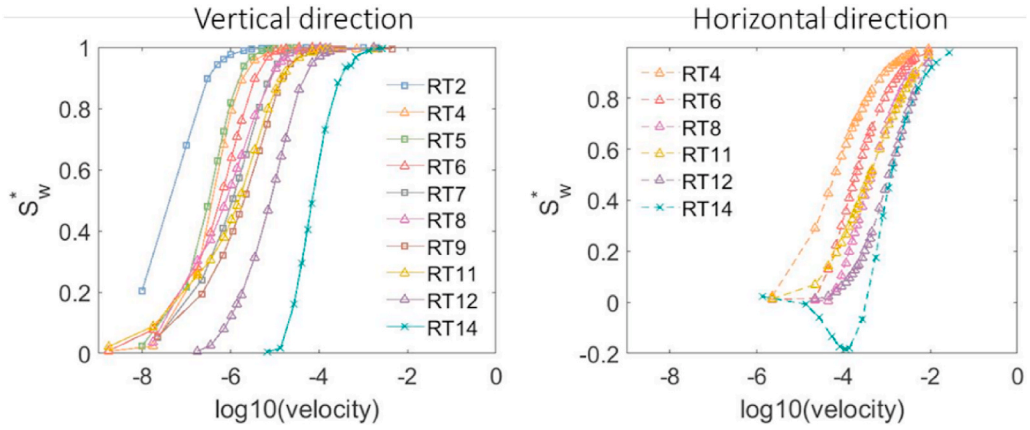

Fig. 10. Normalized saturation (S_w^*) at a fractional flow of 50% water and 50% CO_2 plotted as a function of $\log_{10}$ (velocity)(m/s) for flow in the vertical direction (left) and horizontal direction (right) for each of the different rocktypes. The markers indicate simulation results. When $S_w^* = 0$ the CL is reached, when $S_w^* = 1$ the VL is reached.

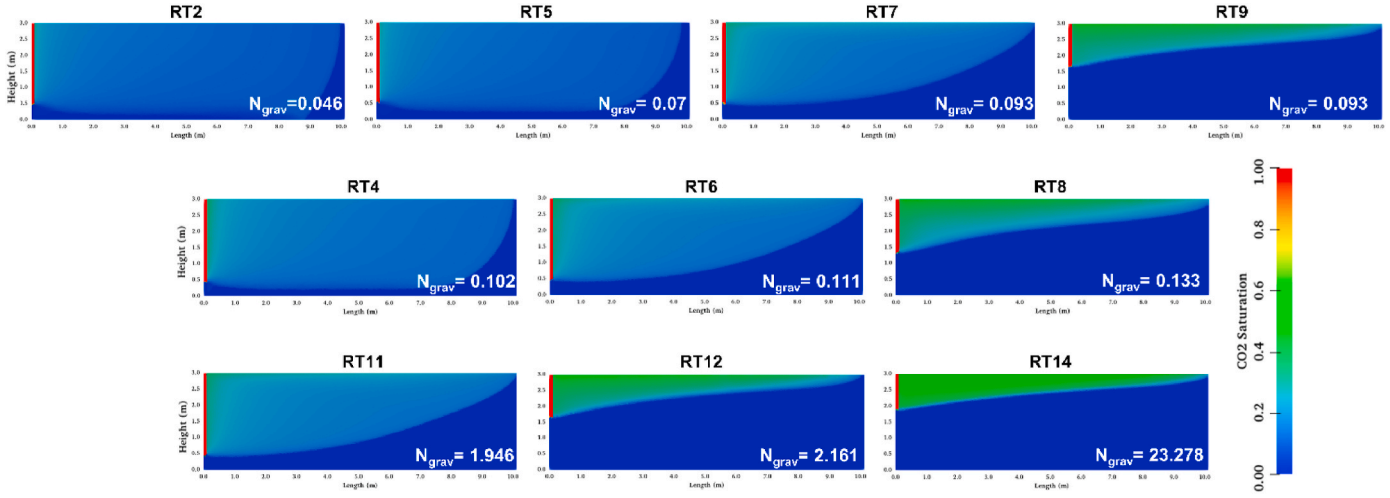

Fig. 11. CO_2 saturation distribution at the time of the breakthrough. Injection through vertical well on left. Force balances reported in terms of gravity number at bottom right of each model.

rocktypes are not flow-rate dependent. The flow-rate dependent behaviour arises in laminated composite rocks because of the interaction between the rocktypes of the composite. This has been observed during physical experiments by several researchers (Manoorkar et al., 2021; Perrin and Benson, 2010; Reynolds and Krevor, 2015) including our own experiments using rock-cores of the Paraatte Fm (Boon et al., 2021). These experimental observations are the motivation for this work. The physical experiments showed that for flow parallel to the bedding layers, the relative permeability of the CO_2 phase increases with decreasing flow rate, while the water relative permeability decreases (Fig. 1). The opposite was observed for flow perpendicular to the bedding layers. The same behaviour can be seen from our numerical experiments in Figs. 7 and 8, confirming that the presented model captures the experimentally observed flow behaviour for laminated systems.

Each rocktype of the composite has its own capillary pressure - saturation relationship. Consequently, capillary gradients can exist between the different rocktypes resulting in a capillary induced flux of water into the low permeable layer and CO_2 into the high permeable layer until the system reaches capillary equilibrium. The transition from the CL to the VL is dependent on the thickness and spacing of the laminations because of the $1/L^2$ scaling of nonlinear capillary diffusion (e.g., Sedaghat and Azizmohammadi, 2018). A qualitative estimate when rate dependence begins, may be obtained from the plot of P_c versus the nonlinear $\left|\frac{dP_c}{ds_w}\right|$ of the component rocktypes (Fig. 12). The coarse sandstone has the steepest capillary pressure – saturation derivative at any capillary pressure as compared with the other members rocktypes. Therefore, composites that contain this coarse sandstone (RT8, RT9, RT12 and RT14) transition at higher velocities.

However, the impact of this capillary heterogeneity on the relative permeability is also dependent on the sedimentary structure, as well as the flow-direction. In this work flow-rate dependent relative permeability and capillary pressure have been analysed for three different sedimentary structures, the massive bedding, planar bedding, and cross-bedding, and for flow in the horizontal and vertical direction. The massive bedded rocktypes are characterized with relatively thick and long lateral extending layers. For flow parallel to these bedding layers, the capillary flux is perpendicular to the flow-direction and capillary equilibrium will be reached after only a short distance along the layer. Furthermore, CO_2 will flow preferentially in the high permeable layers and water through the low permeable layers which limits the interference of flow by the other phase. For flow perpendicular to the bedding layers, the capillary flux is parallel to the flow-direction, and even for relatively low flow-rates the system is pushed out of capillary equilibrium. In this case, both phases have to flow through each of the layers which enhances their interference. This is reflected in the low cross-over points of the water and CO_2 relative permeability curves. Similar behaviour is observed for the planar bedded rocktypes, however, the lateral extend of the layers is shorter than the length of the composite. As a result, flow-rate dependent behaviour will also be observed for the horizontal direction. The cross-bedded rocktype of this work consisted of the fine and coarse sandstone rocktypes. Due to the high permeability of these rocktypes quite similar flow behaviour is observed for both flow directions which makes it difficult to determine the impact of the sedimentary structure.

The anisotropy encountered in the equivalent relative permeability found for the composite rocktypes is widely recognized since the work of Corey and Rathjens (1956); however, to the best of our knowledge all previous studies only investigated limit values (CL or VL. e.g., Pickup et al., 2000) while actual flow conditions may lie between the two limits (e.g., Lohne et al., 2006). This is less involved than the approach taken herein because choosing the limit values ascertains the uniqueness of the saturation distribution. The current analysis moves a step further by considering the full spectrum of potential flow regimes. This is important because the ubiquitous heterogeneity imposed on highly permeable sandstone formations by internal bedforms leads to localised flow and widely varying force balances during CO_2 injection (Matthai and Burney, 2018). That this is also true in the far-field of the well is illustrated in 3D in a companion paper (Shao et al., in review in IJGGC). Our new formulation permits – for the first time - to investigate the implications of such feedbacks between the regional flow regime and the local saturation distributions with a compositional reservoir simulator.

Our new method delivers a new set of constitutive relationships that are continuous, explicit functions in saturation, flow direction and phase velocity magnitude. Achieving an acceptable match between of the numerical simulation results was not an easy task because of the multivariate nature of the problem. The curve fitting faced two major challenges: 1) formulating the fitting functions, and 2) estimating the best fit coefficients for each rock type. The presented strategy selected two fitting functions; Chierici and the well known VanGenuchten, the coefficients of which were made rate dependent. The Chierici formulation which is given by Equations (6) and (7) was first proposed by Chierici (1984) for gas/oil drainage and water/oil imbibition relative permeability curves. Recently, these functions have been used for the CO_2-water system by several authors (Jackson et al., 2018; Benham et al., 2021; Wenck et al., 2021). The parameters can be adjusted to control the shape and curvature of the relative permeability function and therefore provide more flexibility than standard Corey type of equations to fit the data points that were obtained with the numerical

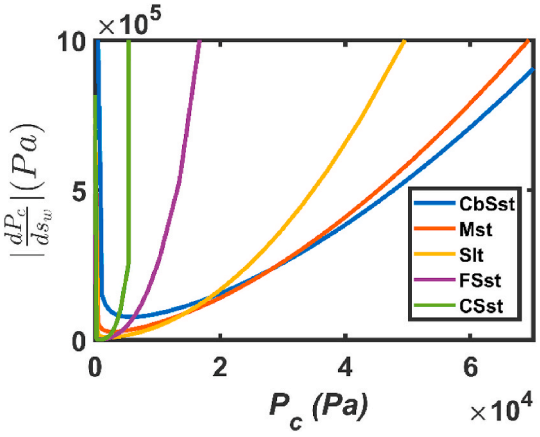

Fig. 12. P_c vs. $\left|\frac{dP_c}{ds_w}\right|$ for the constituent rock types of the composites.

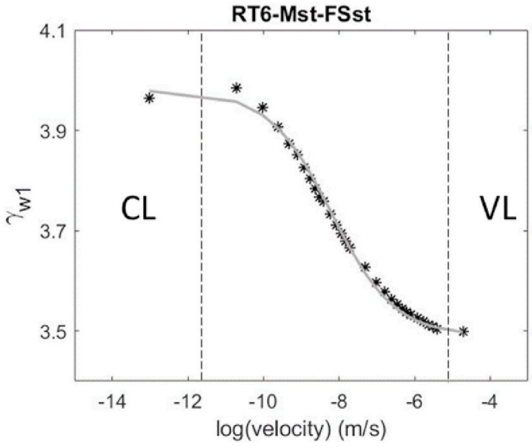

Fig. 13. The scaling of fitting parameter Υ_{w1} of the Chierici formulation for the relative permeability of the water phase (Eq. (6)) for rocktype 6 (RT6) in the transition zone between the CL and VL. The stars show the best fit Υ_{w1} parameter for the relative permeability curves obtained from the numerical coreflood tests for a range of velocities between the VL and the CL, while the solid line shows the Υ_{w1} obtained with Eq. (8) as a function of velocity.

core-flood tests. Eq. (8) is a form of the logistic function and is used to scale the fitting parameters in the transition zone from the viscous limit (VL) to the capillary limit (CL), as can be seen for parameter Υ_{w1} of RT6 in Fig. 13 below.

The main objective of this approach was to simplify implementation and be able to quickly test accuracy and consistency. There are, however, some important issues that need to be resolved in the future:

1) By contrast with the assumption made in classical relative permeability analysis, saturation is non-uniform in heterogeneous porous media. Moreover, the displacement patterns observed and therefore also the relative permeability curves obtained vary with fluid viscosity. Here we only considered fixed viscosity values for water and supercritical CO_2 modelled for the specific injection conditions at Otway (Paterson et al., 2016). Furthermore, dependent on the mobility ratio, displacement is either stable or unstable. The latter manifests in coarsening instabilities producing different saturation patterns which are not captured by the current "steady state" relative permeability analysis (Berg and Ott, 2012). This issue needs to be addressed because it is impractical to carry out additional sensitivity analyses to constrain the effects of fluid properties and under what circumstances such heterogeneity-induced fingering during unstable displacement (Lake, 2010) should or can be adequately captured by adjusting relative permeability. Instead, these should be emergent properties of the reservoir simulation.
2) The behaviour of the anisotropic rate-dependent relative permeability functions is informed only by experiments conducted for two different flow directions. This separation between the two different directions may create inconsistency in the fine scale saturation distribution if the flow is oblique. Eq (18) weighs the effective relative permeability based on the contribution of each direction to the flow. Although this approximation is necessary, it means that k_{rx}^{G} and k_{ry}^{G} values could be generated from two different fine scale saturation distributions. This issue will be studied in the future.
3) The determined equivalent parameters are scale dependent. The scale investigated in this study is 5 cm in the vertical and 1 m in the horizontal direction and was chosen to account for observed differences in correlation length. In addition, the upscaling setup, the resolution and regular discretization of the flow models used, their 2D nature, and the linearization of the flow physics by the simulator will have an impact although we tried to control these factors by application of best modelling practices.

6. Conclusions

This study used numeric multiphase flow simulation to obtain the equivalent CO_2 drainage relative permeability and capillary pressure of ten laminated composite sandstones sampled from the fluvio-estuarine Paaratte formation at CO2CRC's Otway International Test Centre in Victoria, Australia. Flows parallel and perpendicular to the laminae were analysed using an experimental setup and procedure akin to the Penn-State method, where fluids are administered at specific rates and fractional flows through a high-permeability inflow region, and "steady-state" relative permeabilities are extracted when saturation stabilises.

Curve-fitting of the results required different functions for cross-laminar versus laminae-parallel flows indicating a strong directional dependence of relative permeability. Six of the analysed samples also feature rate dependence in both directions while the remaining ones are rate-dependent only in the vertical direction. The transition velocity between these limits is 1.5–3 orders of magnitude wide. Drawing on Chierici's method, we can obtain curve fits of relative permeability for all the analysed samples.

The curve fits constrain a new set of anisotropic functions that describe relative permeability and capillary pressure as a function of brine saturation, flow direction and flow rate. To make these functions suitable for compositional simulation, they were regularised and extended beyond rate-dependent saturation end points so that they can now be applied to the compositional simulation in the CO_2–H_2O–NaCl system. For the first time, these new functions permit an investigation of feedbacks between the reservoir-scale flow regime and bed-scale phase mobility. To illustrate such applications to reservoir simulation, and to demonstrate the robustness of the new approach, meter-scale plume spreading simulations were conducted for the suite of thus homogenised fluvial-to-estuarine sandstones from Otway.

Credit author statement

Maartje Boon: Methodology, Writing - Review & Editing. Stephan K. Matthäi: Methodology, Writing - Review & Editing, Supervision, Funding acquisition. Qi Shao: Methodology, Writing - Review & Editing. AbdAllah A. Youssef: Methodology, Writing - Review & Editing. Achyut Mishra: Resources. Sally M. Benson: Conceptualization, Methodology, Supervision, Funding acquisition.

Declaration of competing interest

The authors declare that they have no known competing financial interests or personal relationships that could have appeared to influence the work reported in this paper.

Acknowledgements

This research was conducted in the frame of GeoCquest, a BHP-funded collaborative research project of the University of Melbourne (Australia), Cambridge University (UK), and Stanford University (USA) as partners. The authors would like to thank CO2CRC for giving access to data from its Otway International Test Centre.

Nomenclature

Latin letters

D	Depth (L)
f	Fractional flow
g	Gravitational acceleration (LT^{-2})
h	Height above free water level (L)
k and $\overline{\overline{k^G}}$	Permeability and permeability tensor at geo-cellular scale (L^2)
k_{rw} and k_{rnw}	Wetting phase relative permeability and non-wetting phase relative permeability
m	The empirical VanGenuchten exponent
N_{grav}	Gravity number
n	Normal unit vector
P, P_c and P_e	Pressure, capillary pressure, and capillary entry pressure ($ML^{-1}T^{-2}$)
s_{wr}, s_{wt} and s_{wt_CL}	Brine saturation, threshold brine saturation and threshold brine saturation at CL

t	Time (T)
u	Velocity vector (LT^{-1})
x	Space vector (L)

Greek letters

φ	Porosity
ρ	Density (ML^{-3})
μ	Dynamic viscosity ($ML^{-1}T^{-1}$)
λ and λ_T	Mobility and total mobility ($M^{-1}LT$)
Ω	Computational space domain
α	Phase (brine or CO_2)

Appendix B. Supplementary data

Supplementary data to this article can be found online at https://doi.org/10.1016/j.petrol.2021.109934.

Appendix A

This appendix summarizes the root mean square (rms) error for all the curve fittings as shown in Fig. A1.

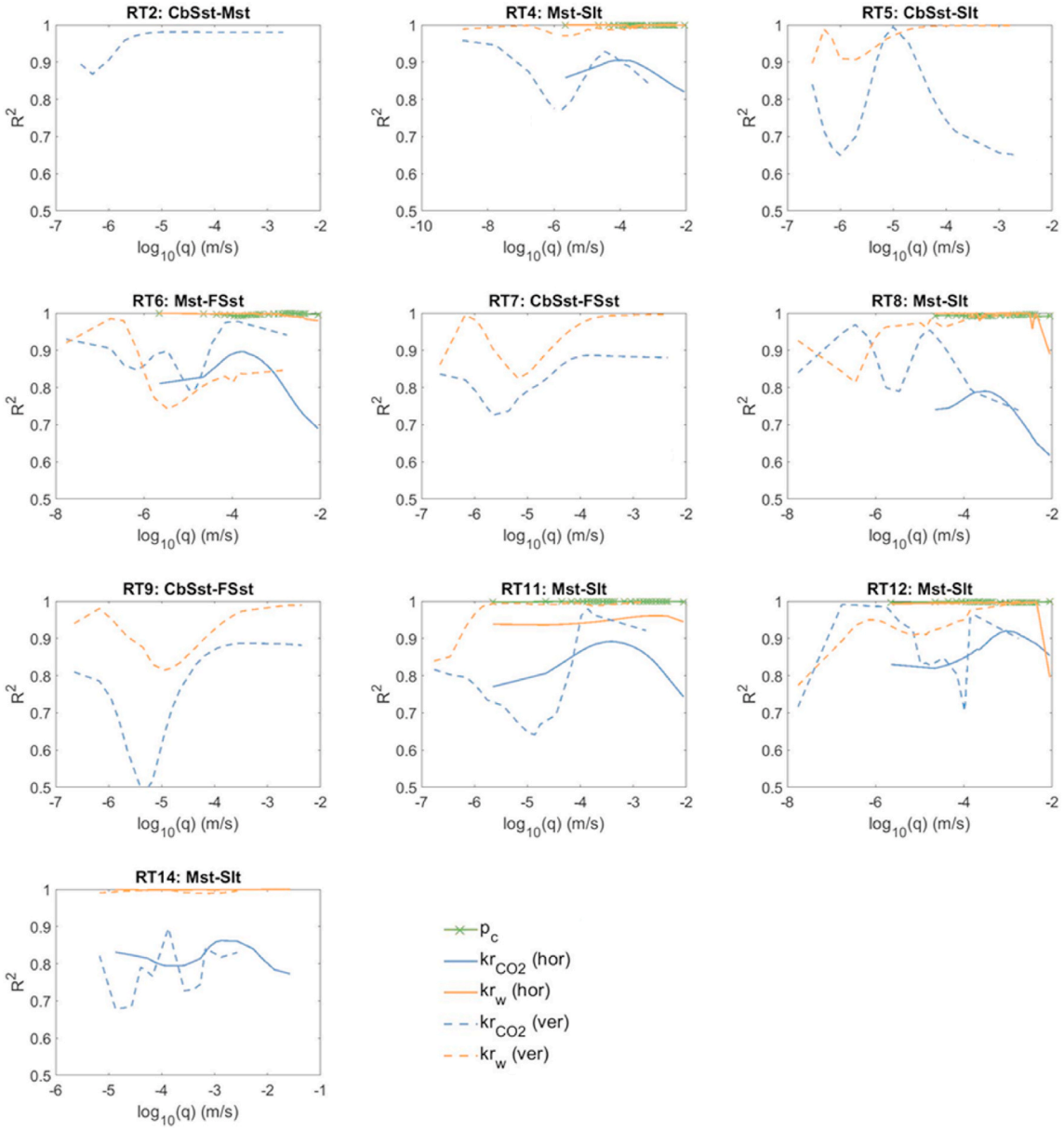

Fig. A1. The mean square error plotted as a function of velocity for all curve fits.

References

Aziz, K., Settari, A., 1979. Petroleum Reservoir Simulation. Appl. Sci. Publ. Ltd., London, UK.

Bazrafkan, S., Matthai, S.K., Mindel, J.E., 2014. The finite-element-centered finite-volume discretization method (FECFVM) for multiphase transport in porous media with sharp material discontinuities. In: 14th European Conference on the Mathematics of Oil Recovery 2014, ECMOR 2014. European Association of Geoscientists and Engineers, EAGE, pp. 1–22. https://doi.org/10.3997/2214-4609.20141841.

Benham, G., Bickle, M., Neufeld, J., 2021. Upscaling multiphase viscous-to-capillary transitions in heterogeneous porous media. J. Fluid Mech. 911, A59. https://doi.org/10.1017/jfm.2020.1134.

Berg, S., Ott, H., 2012. Stability of CO2–brine immiscible displacement. Int. J. Greenh. Gas Control 11, 188–203 https://doi.org/https://doi.org/10.1016/j.ijggc.2012.07.001.

Boon, M., Benson, S.M., 2021. A physics-based model to predict the impact of horizontal lamination on CO2 plume migration. Adv. Water Resour. 150, 103881 https://doi.org/https://doi.org/10.1016/j.advwatres.2021.103881.

Boon, M., Ni, H., Benson, S.M., 2021. Observations of the Impact of MM-Cm Scale Lamination on the Migration and Trapping of CO 2 in Reservoir Rocks. Available SSRN 3820447.

Chen, Z., Huan, G., Ma, Y., 2006. Computational Methods for Multiphase Flows in Porous Media. Society for Industrial and Applied Mathematics. https://doi.org/10.1137/1.9780898718942.

Cheng, C.-L., Perfect, E., Yu, T.E., Gragg, M.J., 2017. Impact of the capillary pressure-saturation pore-size distribution parameter on geological carbon sequestration estimates. J. Sustain. Min. 16, 67–72 https://doi.org/https://doi.org/10.1016/j.jsm.2017.09.001.

Chierici, G.L., 1984. Novel relations for drainage and imbibition relative permeabilities. Soc. Petrol. Eng. J. 24, 275–276.

Coll, C., Muggeridge, A.H., Jing, X.D., 2001. Regional upscaling: a new method to upscale waterflooding in heterogeneous reservoirs for a range of capillary and gravity effects. SPE J. 6, 299–310. https://doi.org/10.2118/74139-PA.

Cook, P., 2014. Geologically Storing Carbon: Learning from the Otway Project Experience. CSIRO publishing.

Corey, A.T., Rathjens, C.H., 1956. Effect of stratification on relative permeability. J. Petrol. Technol. 8, 69–71. https://doi.org/10.2118/744-G.

Dale, M., Ekrann, S., Mykkeltveit, J., Virnovsky, G., 1997. Effective relative permeabilities and capillary pressure for one-dimensional heterogeneous media. Transport Porous Media 26, 229–260. https://doi.org/10.1023/A:1006536021302.

Dance, T., Arnot, M., Bunch, M., Hortlre, A., Lawrence, M., Ennis-King, J., 2012. Geocharacterisation and static modelling ofthe lower Paaratte formation. CO2CRC Otway Project Stage 2.

Dance, T., LaForce, T., Glubokovskikh, S., Ennis-King, J., Pevzner, R., 2019. Illuminating the geology: post-injection reservoir characterisation of the CO2CRC Otway site. Int. J. Greenh. Gas Control 86, 146–157 https://doi.org/https://doi.org/10.1016/j.ijggc.2019.05.004.

Daniel, R., 2012. Containment/Injectivity Results from MICP Analysis for Seals, Intraformational Barriers and Reservoir Samples, CRC-2, Otway Basin. CO2CRC Publ. Number TBN 12-3830; Coop. Res. Cent. Greenh. Gas Technol. Melbourne (Aust).

Daniel, R.F., Menacherry, S., Bunch, M., 2012. Characterisation of Dolomitic Intraformational Barriers. CRC-2B Injection Interval, Paaratte Formation, Melbourne, Australia.

Durlofsky, L.J., 2005. Upscaling and gridding of fine scale geological models for flow simulation. In: 8th International Forum on Reservoir Simulation Iles Borromees, pp. 1–59. Stresa, Italy.

Ekrann, S., Aasen, J.O., 2000. Steady-state upscaling. Transport Porous Media 41, 245–262. https://doi.org/10.1023/A:1006765424927.

Ekrann, S., Dale, M., Langaas, K., Mykkeltveit, J., 1996. Capillary limit effective two-phase properties for 3D media. NPF/SPE Eur. 3-D Reserv. Model. Conf. 119–129 https://doi.org/10.2523/35493-ms.

Fanchi, J.R., 2010. Integrated Reservoir Asset Management Principles and Best Practices.

Geary, G., Reid, I., 1998. Hydrocarbon Prospectivity of the Offshore Eastern Otway Basin, Victoria, for the 1998 Acreage Release. Department of Natural Resources and Environment.

Henderson, G.D., Danesh, A., Tehrani, D.H., Peden, J.M., 1997. The effect of velocity and interfacial tension on relative permeability of gas condensate fluids in the wellbore region. J. Petrol. Sci. Eng. 17 (3–4), 265–273. https://doi.org/10.1016/S0920-4105(96)00048-4. ISSN 0920-4105.

Henderson, G.D., Danesh, A., Tehrani, D.H., 1999. Effect of positive rate sensitivity and inertia on gas condensate relative permeability at high velocity. Brighton,U.K., August 18–20. In: Proceedings of the 10th European Symposium on Improved Oil Recovery.

Henderson, G.D., Danesh, A., Tehrani, D.H., Al-Shaldi, S., Peden, J.M., 1996. Measurement and correlation of gas condensate relative permeability by the steady-state method. SPE J. 1 (2), 191–202.

Hermanson, J., Kirste, D., 2013. Representation of geological heterogeneities and their effects on mineral trapping during CO2 storage using numerical modeling. Procedia Earth Planet. Sci. 7, 350–353 https://doi.org/https://doi.org/10.1016/j.proeps.2013.03.127.

Holtz, M.H., 2002. Residual gas saturation to aquifer influx: a calculation method for 3-D computer reservoir model construction. In: SPE Gas Technology Symposium.

Huppler, J.D., 1970. Numerical investigation of the effects of core heterogeneities on waterflood relative permeabilities. Soc. Petrol. Eng. J. 10, 381–392.

Jackson, S.J., Agada, S., Reynolds, C.A., Krevor, S., 2018. Characterizing drainage multiphase flow in heterogeneous sandstones. Water Resour. Res. 54, 3139–3161. https://doi.org/10.1029/2017WR022282.

Jackson, S.J., Krevor, S., 2020. Small-scale capillary heterogeneity linked to rapid plume migration during CO2 storage. e2020GL088616 Geophys. Res. Lett. 47. https://doi.org/10.1029/2020GL088616.

Jonoud, S., Jackson, M.D., 2008. New criteria for the validity of steady-state upscaling. Transport Porous Media 71, 53–73. https://doi.org/10.1007/s11242-007-9111-x.

Kaldi, J., Daniel, R., Tenthorey, E., Michael, K., Schacht, U., Nicol, A., Underschultz, J., Backe, G., 2011. Caprock systems for CO2 geological storage. IAEGHG Rep 1, 149.

Krause, M.H., Benson, S.M., 2015. Accurate determination of characteristic relative permeability curves. Adv. Water Resour. 83, 376–388. https://doi.org/10.1016/j.advwatres.2015.07.009.

Lake, L.W., 2010. Enhanced Oil Recovery, Enhanced Oil Recovery. https://doi.org/10.1016/C2009-0-30583-8.

Lawrence, M., Arnot, M., Browne, G., Bunch, M., Dance, T., 2013. Geological Interpretation of Core and Wireline Data from Otway Project Wells CRC-1 and CRC-2.

Lohne, A., Virnovsky, G.A., Durlofsky, L.J., 2006. Two-stage upscaling of two-phase flow: from core to simulation scale. SPE J. 11, 304–316. https://doi.org/10.2118/89422-PA.

Manoorkar, S., Jackson, S.J., Krevor, S., 2021. Observations of the impacts of millimeter- to centimeter-scale heterogeneities on relative permeability and trapping in carbonate rocks. Water Resour. Res. 57 e2020WR028597. https://doi.org/https://doi.org/10.1029/2020WR028597.

Matthäi, S.K., Geiger, S., Roberts, S.G., Paluszny, A., Belayneh, M., Burri, A., Mezentsev, A., Lu, H., Coumou, D., Driesner, T., Heinrich, C.A., 2007. Numerical simulation of multi-phase fluid flow in structurally complex reservoirs. Geol. Soc. Spec. Publ. 292, 405–429. https://doi.org/10.1144/SP292.22.

Matthai, Stephan, Burney, Chloe, 2018. Scale-Transgressive Simulation of the Impact of Heterogeneity on Co2 Migration Using High-Resolution Outcrop-Analog Models. In: 14th Greenhouse Gas Control Technologies Conference Melbourne 21-26 October 2018 (GHGT-14). https://doi.org/10.2139/ssrn.3366037. Available at SSRN. https://ssrn.com/abstract=3366037.

Mishra, A., Kurtev, K.D., Haese, R.R., 2020. Composite rock types as part of a workflow for the integration of mm-to cm-scale lithological heterogeneity in static reservoir models. Mar. Petrol. Geol. 114, 104240. https://doi.org/10.1016/j.marpetgeo.2020.104240.

Mishra, A., Pajank, L., Haese, R.R., 2019. High resolution characterization of lithological heterogeneity of the paaratte formation, otway basin(Australia), a coastal to shallow-marine deposit. Geosci. 9 https://doi.org/10.3390/geosciences9060278.

Moreno, Z., Anto-Darkwah, E., Rabinovich, A., 2021. Semi-analytical modeling of rate-dependent relative permeability in heterogeneous formations. Water Resour. Res. 57 e2021WR029710. https://doi.org/https://doi.org/10.1029/2021WR029710.

Mott, R., Cable, A., Spearing, M., 1999. A new method of measuring relative permeabilities for calculating gas-condensate well deliverability. Paper SPE 56484. Houston, October 3–6. In: Proceedings of the SPE Annual Technical Conference and Exhibition.

Mott, R., Cable, A., Spearing, M., 2000. Measurements and simulation of inertial and high capillary number flow phenomena in gas-condensate relative permeability. Paper SPE 62932. Dallas, Texas, October 1-4. In: Proceedings of SPE Annual Technical Conference and Exhibition.

Muskat, M., 1938. The flow of homogeneous fluids through porous media. Soil Sci. 46, 169. https://doi.org/10.1097/00010694-193808000-00008.

Muskat, M., Wyckoff, R.D., Botset, H.G., Meres, M.W., 1937. Flow of gas-liquid mixtures through sands. Trans. AIME 123, 69–96.

Nasriani, H.R., Borazjani, A.A., Iraji, B., MoradiDowlatAbad, M., 2015. Investigation into the effect of capillary number on productivity of a lean gas condensate reservoir. J. Petrol. Sci. Eng. 135, 384–390. https://doi.org/10.1016/S0920-4105(96)00048-4.

Odsæter, L.H., Berg, C.F., Rustad, A.B., 2015. Rate dependency in steady-state upscaling. Transport Porous Media 110, 565–589. https://doi.org/10.1007/s11242-015-0573-y.

Osoba, J.S., Richardson, J.G., Kerver, J.K., Hafford, J.A., Blair, P.M., 1951. Laboratory measurements of relative permeability. J. Petrol. Technol. 3, 47–56.

Paterson, L., Boreham, C., Bunch, M., Dance, T., Ennis-King, J., Freifeld, B., Haese, R., Jenkins, C., LaForce, T., Raab, M., Singh, R., Stalker, L., Zhang, Y., 2013. Overview of the CO2CRC otway residual saturation and dissolution test. Energy Procedia 37, 6140–6148. https://doi.org/10.1016/j.egypro.2013.06.543.

Paterson, L., Ennis-King, J., Freifeld, B., 2016. Monitoring wellbore fluid displacement in the perforation interval using multiple downhole pressure and temperature gauges. In: SPE Asia Pacific Oil and Gas Conference and Exhibition. https://doi.org/10.2118/182456-MS.

Perrin, J.C., Benson, S., 2010. An experimental study on the influence of sub-core scale heterogeneities on CO2 distribution in reservoir rocks. Transport Porous Media 82, 93–109. https://doi.org/10.1007/s11242-009-9426-x.

Pevzner, R., Urosevic, M., Tertyshnikov, K., AlNasser, H., Caspari, E., Correa, J., Daley, T., Dance, T., Freifeld, B., Glubokovskikh, S., Greenwood, A., Kepic, A., Popik, D., Popik, S., Raab, M., Robertson, M., Shulakova, V., Singh, R., Watson, M., Yavuz, S., Ziramov, S., Gurevich, B., 2020. Chapter 6.1 - active surface and borehole seismic monitoring of a small supercritical CO2 injection into the subsurface: experience from the CO2CRC Otway Project. In: Kasahara, J., Zhdanov, M.S., Mikada, H. (Eds.), Active Geophysical Monitoring, second ed. Elsevier, pp. 497–522. https://doi.org/https://doi.org/10.1016/B978-0-08-102684-7.00024-8.

Pickup, G., Ringrose, P.S., Sharif, A., 2000. Steady-state upscaling: from lamina-scale to full-field model. SPE J. 5, 208–217. https://doi.org/10.2118/62811-PA.

Pickup, G.E., Sorbie, K.S., 1996. The scaleup of two-phase flow in porous media using phase permeability tensors. SPE J. 1, 369–382. https://doi.org/10.2118/28586-PA.

Rabinovich, A., Li, B., Durlofsky, L.J., 2016. Analytical approximations for effective relative permeability in the capillary limit. Water Resour. Res. 52, 7645–7667. https://doi.org/10.1002/2016WR019234.

Reynolds, C.A., Krevor, S., 2015. Characterizing flow behavior for gas injection: relative permeability of CO2-brine and N2-water in heterogeneous rocks. Water Resour. Res. 51, 9464–9489. https://doi.org/10.1002/2015WR018046.

Ringrose, P.S., 2008. Total-Property Modeling: dispelling the Net-to-Gross Myth (see associated supplementary discussion and response). SPE Reservoir Eval. Eng. 11, 866–873.

Ringrose, P.S., Jensen, J.L., Sorbie, K.S., 1996. Use of geology in the interpretation of core-scale relative permeability data. SPE Form. Eval. 11, 171–176. https://doi.org/10.2118/28448-PA.

Ringrose, P.S., Sorbie, K.S., Corbett, P.W.M., Jensen, J.L., 1993. Immiscible flow behaviour in laminated and cross-bedded sandstones. J. Petrol. Sci. Eng. 9, 103–124. https://doi.org/10.1016/0920-4105(93)90071-L.

Modelling CO_2 plume spreading in highly heterogeneous rocks with anisotropic, rate-dependent saturation functions: A field-data based numeric simulation study of Otway. Qi Shao, Maartje Boon, AbdAllah Youssef, Stephan K. Matthai, Kuncho Kurtev, and Sally M. Benson. Under review in IJGGC.

Sharma, S., Cook, P., Jenkins, C., Steeper, T., Lees, M., Ranasinghe, N., 2011. The CO2CRC Otway Project: leveraging experience and exploiting new opportunities at Australia's first CCS project site. Energy Procedia 4, 5447–5454. https://doi.org/10.1016/j.egypro.2011.02.530.

Spiteri, E.J., Juanes, R., Blunt, M.J., Orr, F.M., 2008. A new model of trapping and relative permeability hysteresis for all wettability characteristics. SPE J. 13, 277–288.

Stüben, K., 2007. Solving reservoir simulation equations. 9th Int. Forum Reserv. Simul. December 53.

Wenck, N., Jackson, S.J., Manoorkar, S., Muggeridge, A., Krevor, S., 2021. Simulating core floods in heterogeneous sandstone and carbonate rocks. Water Resour. Res. 57, e2021WR030581 https://doi.org/10.1029/2021WR030581.

Xu, T., Sonnenthal, E., Spycher, N., Pruess, K., 2008. TOUGHREACT User's Guide: A Simulation Program for Non-isothermal Multiphase Reactive Geochemical Transport in Variably Saturated Geologic Media. V1. 2.1.

Ziesch, J., Aruffo, C.M., Tanner, D.C., Beilecke, T., Dance, T., Henk, A., Weber, B., Tenthorey, E., Lippmann, A., Krawczyk, C.M., 2017. Geological structure and kinematics of normal faults in the Otway Basin, Australia, based on quantitative analysis of 3-D seismic reflection data. Basin Res. 29, 129–148. https://doi.org/10.1111/bre.12146.